Closed-Loop Process Design for Destruction and Resource Recovery of Polyethylene Microplastics via Plasma-Assisted Oxidative Gasification

Shiddharth Tiwari

ORCID: 0009-0002-7308-3495

Department of Chemistry, KJ Somaiya College of Science and Commerce, Mumbai, Maharashtra, India

Email: siddharth70286@gmail.com

Abstract

Polyethylene (PE) microplastic remediation requires approaches that address polymer destruction alongside the management of associated contaminants and conversion products. This study proposes an integrated process for PE-equivalent feed conversion and resource recovery, combining plasma-assisted surface activation, oxygen-assisted oxidative gasification, two-stage water-gas shift (WGS), pressure-swing adsorption (PSA), calcium hydroxide-based CO_2 capture, and heavy-metal precipitation, with optional graphene oxide nanofiltration. The connected equilibrium gas phase prediction under vapor only constraint, WGS, and separation stages were modeled in DWSIM, while the plasma, carbonation, and precipitation stages were evaluated through stoichiometric and literature-based calculations. At an equivalence ratio of 0.30 and 773.15 K, the equilibrium gasification model predicted a product gas containing 40.55 mol% CH_4, 29.43 mol% CO_2, 20.57 mol% CO, and 7.38 mol% H_2. The idealized PSA-equivalent separation produced a hydrogen rich stream containing 50.36 mol% H_2. Downstream calculations yielded 2.611 kg/s of $CaCO_3$ and approximately 0.596 g/s of Zn, Cu, and Pb hydroxide precipitates on the selected feed and contamination basis. The summed stage duty was negative under both evaluated plasma-energy scenarios, indicating modeled net thermal release rather than demonstrated electrical power export. The results establish a simulation-based process design framework; experimental validation and further reactor-level and scale-up assessment remain necessary.

Keywords- Polyethylene microplastics; plasma-assisted oxidative gasification; process simulation; water-gas shift reaction; hydrogen recovery; carbon dioxide capture; resource recovery

1. Introduction

Polyethylene (PE) is the most widely produced plastic globally, and its degradation products — microplastics and, increasingly, nanoplastics — are now recognized as a persistent environmental contaminant across marine, freshwater, and terrestrial systems. Unlike bulk plastic waste, microplastics resist conventional collection and mechanical recycling: their small size, buoyancy or suspension behavior, and chemical inertness make them effectively invisible to existing waste-management infrastructure . Once weathered, PE microplastics undergo surface photo-oxidation that further complicates their removal, generating charged, colloidally stable "nanoplastic" fragments that evade standard filtration [1,2].

Existing remediation approaches fall broadly into two categories: physical separation (filtration, density separation, flotation) and thermochemical destruction (pyrolysis, incineration). Physical separation methods do not destroy the polymer — they relocate it, typically producing a concentrated microplastic-laden sludge that still requires downstream disposal. Thermochemical destruction methods, particularly conventional pyrolysis, destroy the polymer but are energy-intensive, and pyrolysis of PE specifically produces a mixture of long-chain hydrocarbons and waxes with limited direct utility, along with releasing associated heavy-metal and additive contaminants without a defined capture pathway [3-7].

This paper proposes a **closed-loop, multi-stage process** that treats PE microplastics as a feedstock rather than only as a waste stream to be filtered out. The design integrates plasma-assisted surface activation, oxidative gasification, syngas upgrading via water-gas shift and pressure-swing adsorption, and downstream capture of both carbon dioxide and heavy-metal byproducts, *with an optional final nanosheet-based polishing stage. This optional stage — amine-functionalized graphene oxide (GO) nanofiltration — is not required for the core mass and energy balance reported in this work, but is included for researchers seeking additional assurance against residual nanoplastic or colloidal metal-hydroxide carryover during physical replication; its inclusion is grounded in established literature on GO-based microplastic capture [8-10] and amine-functionalized adsorbent design [11]. Each individual unit operation — plasma treatment of polyolefins [12,13] , oxidative gasification [16-20], water-gas shift for hydrogen production [21-23], alkaline ($Ca(OH)_2$) capture of CO_2 [24-25], and hydroxide precipitation of heavy metals [26] — has established precedent in the literature*. The contribution of this work is not any single mechanism but the **specific end-to-end integration of these steps for PE microplastic destruction**, evaluated through a process simulation (DWSIM) with a closed mass and

energy balance, which was not found assembled as a single pipeline in the literature surveyed for this paper.

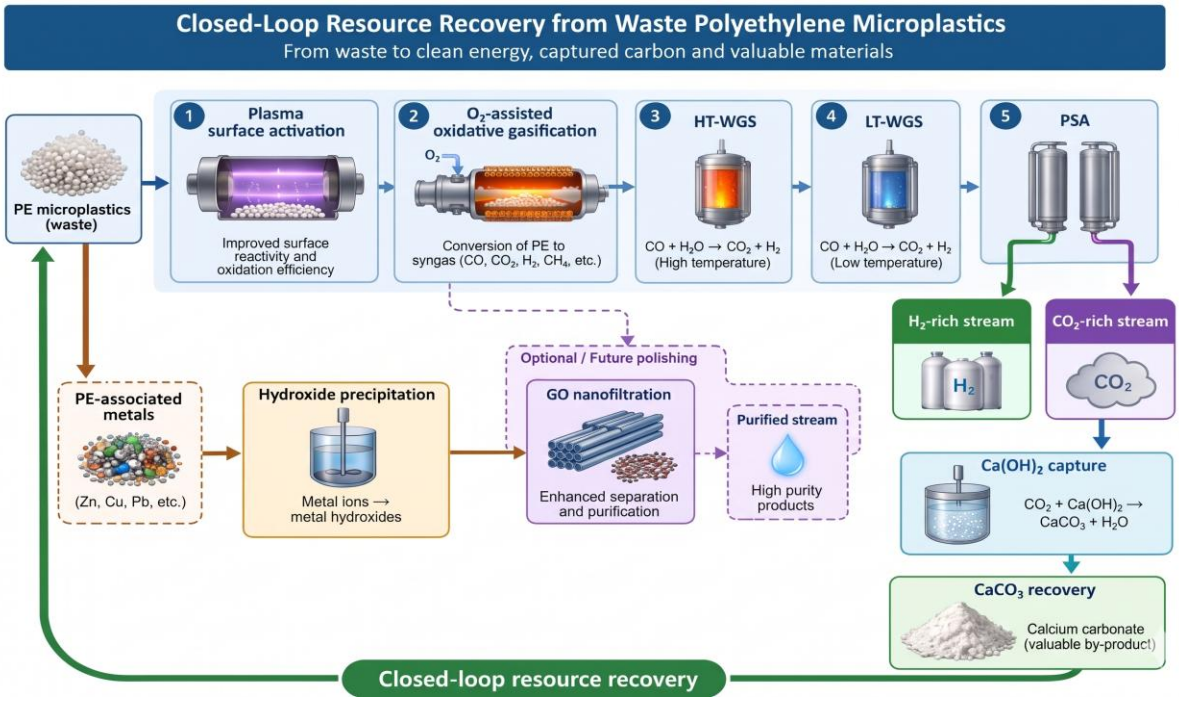


Figure 1. Schematic representation of the proposed closed-loop process for destruction and resource recovery of polyethylene microplastics. The process integrates plasma surface activation, oxygen-assisted oxidative gasification, two-stage water-gas shift, pressure-swing adsorption, CO_2 capture as $CaCO_3$, heavy-metal precipitation, and an optional graphene oxide nanofiltration polishing stage.

Specifically, this paper:

1. Proposes and justifies a six-stage (plus one optional) process pipeline for converting PE microplastics into hydrogen-rich syngas, captured CO_2 (as $CaCO_3$), precipitated heavy metals, and — optionally — a polished water stream free of residual nano-scale particulates.
2. Presents a corrected process simulation in DWSIM, including an explicit discussion of assumptions revised during development, rather than presenting only a final idealized result.
3. Reports stage-wise material accounting and calculated energy duties across the modeled process, including a comparative assessment of the two plasma-energy scenarios.

4. Identifies the principal modeling and scale-up considerations associated with the proposed design, including the selected heavy-metal basis, assumptions requiring further simulation verification, and the batch-to-continuous scaling applied to the plasma-energy estimate.

2. Background and Related Work

2.1 Physical vs. Thermochemical Remediation of PE Microplastics

Existing approaches to microplastic remediation split into two categories, both with structural limitations this work aims to address. Physical separation methods — filtration, density separation, flotation — do not destroy the polymer; they transfer it into a concentrated reject or sludge stream that requires subsequent management or treatment. Thermochemical destruction, particularly conventional inert-atmosphere pyrolysis, does destroy the polymer but is energy-intensive and, for PE specifically, yields a product slate of long-chain hydrocarbons and waxes with limited direct utility, while releasing associated heavy-metal and additive contaminants without a defined capture pathway. This motivates a design that treats destruction and resource recovery as a single integrated problem rather than two separate ones [1,3-4,8].

2.2 Plasma-Assisted Polymer Treatment

Cold plasma treatment of polyolefin surfaces is established as a means of both introducing reactive oxygen-containing functional groups and accelerating subsequent thermal decomposition [12-13]. Diaz-Silvarrey et al. (2018) [4] found that ethylene recovery from polyethylene pyrolysis, when preceded by cold plasma-catalysis, was up to 55 times higher than recovery from conventional pyrolysis alone, with no additional heating input. This establishes plasma pretreatment's role as a kinetics enhancer rather than a stoichiometric reactant — a distinction this work relies on directly (see Section 6.1). Complementary work on oxygen RF plasma treatment of polyethylene, characterized via XPS, confirms that plasma exposure introduces carboxyl and peroxide surface groups, with peroxide concentration rising with exposure time up to an optimum before overexposure shifts the product distribution toward additional C=O bonds [12]. This provides a mechanistic basis for Stage I of the proposed design (Section 3.1): plasma-induced surface oxidation and functionalization can alter the surface chemistry of polyethylene and may influence its subsequent thermal reactivity during Stage II.

2.3 Oxidative Gasification of Plastics

Partial oxidation gasification of plastic waste is governed by the equivalence ratio (ER), the ratio of actual to stoichiometric oxidant supply. Gasification performance is strongly influenced by the equivalence ratio (ER), with reported favorable operating conditions varying with feedstock, oxidant, temperature, reactor configuration, and the performance metric considered. An ER of 0.30 falls within the range investigated for plastic and polymer-containing gasification systems and was therefore selected as the operating condition for Stage II in the present integrated process design. Oxygen (as opposed to air) gasification further enhances carbon conversion and yields syngas with substantially higher H_2 and CO concentrations relative to air-blown gasification, though PE specifically is documented to produce comparatively higher CH_4 concentrations under oxygen gasification due to the fast cracking behavior of the polymer. This literature provides the operating context for the ER selected in the present design and provides a basis for interpreting the CH_4-rich product distribution obtained from Stage II [16-20]. It is important to note that the present work does not attempt to reproduce these experimental gasifier results directly . Stage 2 is modeled as a Gibbs free-energy equilibrium calculation undra vapor-only constraint (section 4.3) , and therefore represents a thermodynamic idealization rather than a prediction of kinetically limited reactor. The literature is used here only to justify the selected equivalence ratio and to contextualize the methane-rich equilibrium distribution, not to validate the stage 2 model against experimental gasifier performance.

2.4 Water-Gas Shift for Hydrogen Production

Industrial hydrogen production from syngas conventionally employs a two-stage water-gas shift (WGS) configuration to maximize CO conversion (via reaction with steam) to H_2 and CO_2, while respecting the reaction's thermodynamic equilibrium constraints. A high-temperature stage, typically operated between 310-450°C over an iron-oxide/chromium-oxide catalyst, reduces CO to the range of 1-5%; a subsequent low-temperature stage, operated between 200-250°C over a copper/zinc-oxide catalyst, further reduces CO to below 0.5% [21-23]. This two-stage architecture is adopted directly in Stage III of the proposed design (Section 3.3); the correspondence between this work's simulated outlet CO concentrations and these literature targets is addressed in the Discussion (Section 6.3), alongside a noted deviation in operating temperature [21,23].

2.5 Lime-Based CO_2 Capture

Calcium hydroxide slurry — industrially termed "milk of lime" when prepared as an aqueous suspension — is an established sorbent for CO_2 capture from process and flue gas streams. Pilot-scale moving-bed studies have demonstrated CO_2 capture rates exceeding 99% using $Ca(OH)_2$/CaO sorbents under simulated flue gas conditions, with molar conversion to $CaCO_3$ of approximately 0.7, at CO_2 concentrations up to 8.5% [24-25]. This establishes lime-slurry capture as a demonstrated, not merely theoretical, unit operation, and directly supports Stage V of the proposed design (Section 3.5); the applicability of these benchmarks to this work's substantially higher CO_2 concentration (36.93%) is discussed in Section 6.4 [24-25].

2.6 Heavy Metals on Microplastics and Hydroxide Precipitation

Microplastics, including PE, are established vectors for heavy-metal adsorption from their environment [7]. Reported concentrations of Zn and Cu in PE-based plastic materials provide an upper-end contamination basis of 365.9 and 184.2 mg/kg, respectively, for the present process calculation. A representative Pb concentration of approximately 10 mg/kg was also adopted from reported PE/HDPE concentration ranges [5-6]. Hydroxide precipitation — raising pH to 9-10 via NaOH or $Ca(OH)_2$ addition to precipitate metal hydroxides — is a standard, well-characterized treatment approach for such contamination, and forms the basis of Stage VI in the proposed design (Section 3.6) [26]. Cadmium and chromium have been reported in plastic materials [5-6], but they were not included in the selected quantitative contamination basis used for the present precipitation calculation.

2.7 Amine-Functionalized Graphene Oxide for Nanoplastic Capture (Optional Stage)

Environmental weathering can alter the surface properties and dispersibility of polyethylene-based microplastics, potentially influencing their transport and persistence in aqueous systems [1-2]. Graphene oxide (GO)-based membranes have demonstrated potential for micro/nanoplastic removal in water-treatment applications, including recent experimental work reporting high microplastic removal using a GO-based composite membrane [8-10]. Surface functionalization provides an additional mechanism for controlling interactions between GO and nanoplastics. Recent molecular-dynamics simulations of alkylamine-functionalized GO showed enhanced binding of polyethylene terephthalate (PET) and polystyrene (PS) nanoplastics through combined hydrophobic and π–π interactions, whereas polypropylene (PP) exhibited weaker and less specific

adsorption [11]. In addition, the interlayer spacing of GO membranes can be regulated through approaches such as pressure control and chemical modification, providing a means of tuning membrane transport properties [14-15]. Together, this literature supports the investigation of functionalized GO as a potential downstream polishing material for residual micro/nanoplastic contaminants, while recognizing that rejection and transport behavior must be established for the specific PE-containing system proposed here. The proposed application is therefore treated as an optional stage for physical replication rather than as a quantitatively validated component of the core mass and energy balance reported in this work.

3. Process Description

The proposed design comprises six sequential stages plus one optional final stage, converting a continuous PE microplastic feed into hydrogen-containing product gas, recovered $CaCO_3$, precipitated heavy metals, and — optionally — a membrane-polished aqueous stream. A schematic of the full pipeline is given in Figure 1; detailed simulation parameters and stream-level results are reported in Sections 4 and 5 respectively. This section describes the function, chemistry, and rationale of each stage in sequence.

3.1 Stage I — Cold Pulsed Plasma Pretreatment

The PE microplastic feed first undergoes cold pulsed plasma treatment, using a 10-30 kV pulsed discharge. This stage performs surface activation rather than bulk polymer conversion, introducing oxygen-containing functional groups onto the PE surface and modifying its surface chemistry prior to Stage II [12-13]. The plasma's pulsed operation keeps energy input low relative to continuous discharge modes, an important consideration given the specific energy requirement quantified in Section 5. The role of this stage is to modify the surface chemistry of the feed and potentially influence its subsequent thermal reactivity in Stage II.

3.2 Stage II — Oxidative Gasification

The plasma-activated PE feed proceeds to oxidative gasification, where it is reacted with a metered oxygen supply at the selected equivalence ratio (ER) of 0.30, as established in the process design and discussed in Section 2.3. Operating at 773.15 K under oxygen-limited (sub-stoichiometric) conditions, the equilibrium model predicts conversion of the PE-equivalent feed into a product-gas mixture dominated by CH_4, CO_2, CO, and H_2, with water as a minor co-product [16-20]. This stage represents the destructive core of the process —

the point at which the polymer's carbon backbone is broken down into small, individually tractable molecules — and its output composition is the single most consequential result in the simulation, since every downstream stage operates on this stream. Section 4 details the specific reactor formulation and feed representation used to model this stage; Section 5 reports the resulting composition; Section 6.2 compares it against the literature benchmarks introduced in Section 2.3.

3.3 Stage III — Two-Stage Water-Gas Shift

The Stage II syngas, still containing appreciable CO, is upgraded via a two-stage water-gas shift (WGS) train, matching the industrial configuration described in Section 2.4 [21-23]. In the first stage, the syngas is combined with steam and reacted at high temperature using an Fe-based catalyst basis, while the subsequent low-temperature stage uses a Cu-based catalyst basis. The partially shifted stream is then combined with a second steam addition and passed through a low-temperature stage using the Cu-based catalyst basis. This two-stage arrangement exists specifically to overcome the WGS reaction's unfavorable high-temperature equilibrium (which favors reactant CO) while still benefiting from high-temperature reaction kinetics — the high-temperature stage does the bulk of the conversion quickly, and the low-temperature stage pushes the remaining CO down further, closer to the reaction's more favorable low-temperature equilibrium [21-23].

3.4 Stage IV — Pressure-Swing Adsorption Separation

The shifted syngas, now hydrogen-rich, is separated via pressure-swing adsorption (PSA) equivalent separation (modeled as an idealized component separator approximation) into two streams: a hydrogen-rich product stream and a CO_2-rich stream. The H_2-rich stream represents the primary modeled hydrogen-containing product of the process, while the CO_2-rich stream is routed onward for capture and fixation in Stage V. Residual CH_4, unreacted by the WGS stages (which act only on CO and H_2O), is distributed between both streams and is discussed as a process limitation in Section 6.2. This model represents an idealized split of the gas components; detailed adsorption isotherms, pressure swing cycling, regeneration, and kinetics were not modeled in this work.

3.5 Stage V — CO_2 Capture via Calcium Hydroxide Slurry

The CO_2-rich stream from Stage IV is contacted with a calcium hydroxide slurry ("milk of lime," per the industrial terminology established in Section 2.5), where CO_2 is fixed as solid calcium carbonate via the reaction $Ca(OH)_2 + CO_2 \rightarrow CaCO_3 + H_2O$ [24-25]. This stage

provides the carbon-recovery pathway of the process: rather than venting the modeled CO_2 stream, it is converted into recoverable solid $CaCO_3$, with water generated as a byproduct. The resulting slurry proceeds to Stage VI's filtration step for solid-liquid separation and recovery of the $CaCO_3$ product.

3.6 Stage VI — Heavy Metal Precipitation

In parallel with carbon capture, the process addresses the heavy-metal contamination inherent to environmental PE microplastics (established in Section 2.6). The relevant process stream is dosed with NaOH or $Ca(OH)_2$ to raise pH to 9-10, precipitating dissolved heavy metals — principally zinc, copper, and lead in this work's quantified basis — as their corresponding metal hydroxides [26]. The precipitate is recovered by filtration for subsequent stabilization, characterization, recovery, or regulated disposal as appropriate.

3.7 Stage VII (Optional) — Amine-Functionalized Graphene Oxide Nanofiltration

As an optional final stage, the process includes provision for amine-functionalized graphene oxide (GO) nanofiltration, positioned after Stage VI as a downstream polishing step. This stage is not required for the core mass and energy balance reported in this work (Section 5), but is included as a precautionary polishing step for researchers physically replicating the design who wish to guard against two possible carryover scenarios: residual nanoplastic particles surviving Stage II and colloidal metal-hydroxide fines escaping Stage VI filtration. GO-based composite membranes have demonstrated high microplastic removal performance [8-10], while functionalized GO provides an additional surface-chemistry-based mechanism for interactions with nanoplastics [11]. Accordingly, the proposed Stage VII is treated as an optional polishing concept rather than a quantitatively validated membrane unit. Its actual rejection efficiency would require experimental validation under the conditions of the integrated process, including consideration of membrane architecture, surface functionalization, particle characteristics, fouling, and operating conditions [8-11,14-15].

4. Methodology and Simulation Setup

4.1 Simulation Environment

The process was modeled in DWSIM using the Peng-Robinson (PR) property package throughout. Stages II-IV were simulated as a connected flowsheet; Stages I, V, and VI were

evaluated via closed-form stoichiometric and literature-based calculation, detailed in Sections 4.6-4.8.

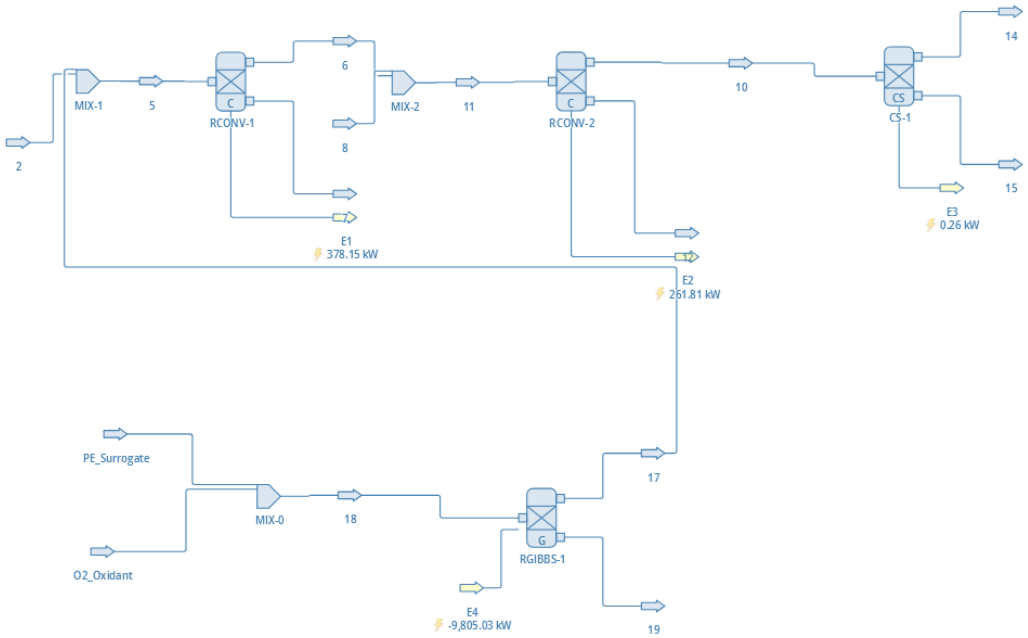


Figure 2. DWSIM flowsheet used to simulate the connected gasification, water-gas shift, and separation stages of the proposed process.

4.2 Feed Representation

DWSIM lacks native thermodynamic data for polyethylene as a polymer species. PE was therefore represented by its elemental-equivalent surrogate, ethylene (C_2H_4), which shares PE's repeat-unit empirical formula $(CH_2)_n$. This representation enables equilibrium process calculation using a molecular surrogate for the elemental composition of PE; it does not represent the detailed polymer-chain reaction mechanism.

Table 1. Feed stream specification (Stage II inlet)

Stream	Species	Molar flow (mol/s)	Molar mass (g/mol)	Mass flow (g/s)
PE-surrogate	C_2H_4	25.00	28.05	701.25
Oxidant	O_2	22.50	32.00	720.00
Total Stage II feed				**1421.25 (1.421 kg/s)**

The PE-equivalent mass (701.25 g/s ≈ 0.701 kg/s) is used as the basis for Stage I and Stage VI calculations (Sections 4.7, 4.8), since these operate on the raw polymer before oxidant addition; the combined 1.421 kg/s figure applies only to Stage II onward.

Equivalence ratio (ER) derivation:

The complete stoichiometric oxidation of the ethylene surrogate is:

$C_2H_4 + 3O_2 \rightarrow 2CO_2 + 2H_2O$

For 25.00 mol/s of C_2H_4:

O_2,stoich = 25.00 × 3 = 75.00 mol/s

The equivalence ratio (ER) is calculated as:

ER = O_2,actual / O_2,stoich

ER = 22.50 / 75.00 = 0.30

Therefore, the selected gasification condition corresponds to an **equivalence ratio of 0.30**.

4.3 Stage II — Gibbs Reactor Configuration

Table 2. RGIBBS-1 operating parameters

Parameter	Value
Reactor type	Gibbs free-energy minimization (RGIBBS)
Temperature	773.15 K
Pressure	101,325 Pa
Reactive phase behavior	Vapor only
Candidate products	CH_4, CO, CO_2, H_2, H_2O, C_2H_4 (unreacted)
Convergence	IPOPT solver, error tolerance 1×10^{-8}

4.4 Stage III — Water-Gas Shift Reactor Configuration

Table 3. RCONV-1 (HT-WGS) and RCONV-2 (LT-WGS) parameters

Parameter	RCONV-1 (HT)	RCONV-2 (LT)

Temperature	773.15 K	473.15 K
Catalyst	Fe-based	Cu-based
Reaction	$CO + H_2O \rightarrow CO_2 + H_2$	$CO + H_2O \rightarrow CO_2 + H_2$
Conversion (specified)	90%	90%
Steam addition	Stream 5	Stream 10

Total steam addition across both stages was 0.80 kg/s (back-calculated via elemental hydrogen/carbon conservation across Stages II-IV; see Section 6.6 for verification status).

4.5 Stage IV — PSA Separation

The PSA stage was represented in DWSIM using a component-separator approximation (CS-1). The model therefore represents an idealized separation step rather than detailed adsorption-cycle behavior, and no adsorbent isotherms, pressure-swing cycling, regeneration, or adsorption kinetics were modeled. Because the PSA stage is modeled as an idealized separator, the reported H_2-rich and CO_2-rich stream compositions represent a theoretical thermodynamic split, not the performance of a real adsorbent bed.

4.6 Stage V — $Ca(OH)_2/CO_2$ Stoichiometric Calculation

Reaction: $Ca(OH)_2 + CO_2 \rightarrow CaCO_3 + H_2O$

Table 4. Molar masses used

Species	Molar mass (g/mol)
CO_2	44.0095
$Ca(OH)_2$	74.0927
$CaCO_3$	100.0869
H_2O	18.0153

Step 1 — CO_2 mass flow

The CO_2-rich stream (Stream 15) has a total molar flow of 70.7307 mol/s. The CO_2 mass flow reported by DWSIM is 1.1495063 kg/s. This reported mass flow is used as the basis for the subsequent stoichiometric calculations.

CO_2 mass flow = 1.1495063 kg/s = 1149.5063 g/s

The corresponding CO_2 molar flow is calculated using the molar mass of CO_2:

$\dot{n}(CO_2) = 1149.5063 / 44.0095$

$\dot{n}(CO_2) = 26.1195037435$ mol/s

Step 2 — $Ca(OH)_2$ required

The carbonation reaction is assumed to proceed with a 1:1 molar ratio between CO_2 and $Ca(OH)_2$. Therefore:

$\dot{n}[Ca(OH)_2] = \dot{n}(CO_2)$

The required $Ca(OH)_2$ mass flow is calculated using its molar mass of 74.0927 g/mol:

$\dot{m}[Ca(OH)_2] = 26.1195037435 \times 74.0927$

$\dot{m}[Ca(OH)_2] = 1935.264555$ g/s

$\dot{m}[Ca(OH)_2] = 1.935264555$ kg/s

Step 3 — $CaCO_3$ produced

The reaction assumes a 1:1 molar ratio between CO_2 consumed and $CaCO_3$ produced. Using the molar mass of $CaCO_3$ (100.0869 g/mol):

$\dot{n}(CaCO_3) = \dot{n}(CO_2)$

$\dot{m}(CaCO_3) = 26.1195037435 \times 100.0869$

$\dot{m}(CaCO_3) = 2614.220159$ g/s

$\dot{m}(CaCO_3) = 2.614220159$ kg/s

Step 4 — H_2O produced

The reaction produces one mole of H_2O per mole of CO_2 consumed. Using the molar mass of H_2O (18.0153 g/mol):

$\dot{n}(H_2O) = \dot{n}(CO_2)$

$\dot{m}(H_2O) = 26.1195037435 \times 18.0153$

$\dot{m}(H_2O)$ = 470.550696 g/s

$\dot{m}(H_2O)$ = 0.470550696 kg/s

Mass-balance check

The total input mass flow comprises CO_2 and $Ca(OH)_2$:

$\dot{m}(in) = \dot{m}(CO_2) + \dot{m}[Ca(OH)_2]$

$\dot{m}(in)$ = 1.1495063 + 1.935264555

$\dot{m}(in)$ = 3.084770855 kg/s

The total output mass flow comprises $CaCO_3$ and the water produced by the reaction:

$\dot{m}(out) = \dot{m}(CaCO_3) + \dot{m}(H_2O)$

$\dot{m}(out)$ = 2.614220159 + 0.470550696

$\dot{m}(out)$ = 3.084770855 kg/s

Thus, the calculated input and output mass flow rates are equal:

$\dot{m}(in) = \dot{m}(out)$ = 3.084770855 kg/s

The mass balance closes using the consistent molar masses listed in Table 4 and the unrounded intermediate calculations. The $Ca(OH)_2$ requirement, $CaCO_3$ production rate, and reaction-generated water flow are stoichiometrically calculated values; they are not direct DWSIM stream outputs.

4.7 Stage VI — Heavy Metal Precipitation Dosing Calculation

Basis: 0.701 kg/s PE-equivalent feed. Contamination levels adopted from Section 2.6: Zn 365.9 mg/kg, Cu 184.2 mg/kg, Pb 10 mg/kg.

Table 5. Contaminant mass and molar flow

Metal	mg/kg	Mass flow (g/s)	Atomic mass (g/mol)	Molar flow (mol/s)
Zn	365.9	0.2561	65.38	0.003918
Cu	184.2	0.1289	63.55	0.002029

Pb	10.0	0.0070	207.2	0.0000338

Reaction: $M^{2+} + 2OH^- \rightarrow M(OH)_2$ (2 mol OH^- per mol metal)

$$\dot{n}_{OH^-} = 2 \times (0.003918 + 0.002029 + 0.0000338) = 0.011962 \text{ mol/s}$$

NaOH dosing (1 mol OH^- per mol NaOH, M = 40.00 g/mol):

$$\dot{m}_{NaOH} = 0.011962 \times 40.00 = 0.4785 \text{ g/s}$$

Alternative — $Ca(OH)_2$ dosing (2 mol OH^- per mol, M = 74.09 g/mol):

$$\dot{m}_{Ca(OH)_2} = 0.0119622 \times 74.09 = 0.4432 \text{ g/s}$$

Table 6. Precipitate mass produced

Precipitate	Molar flow (mol/s)	M (g/mol)	Mass flow (g/s)
$Zn(OH)_2$	0.003918	99.40	0.3895
$Cu(OH)_2$	0.002029	97.57	0.1980
$Pb(OH)_2$	0.0000338	241.2	0.0082
Total			**≈ 0.596**

Cadmium and chromium are not included in the present quantitative precipitation calculation; the selected contamination basis is restricted to Zn, Cu, and Pb.

4.8 Stage I — Plasma Energy Calculation

Specific energy input adopted from Šourková and Špatenka (2020): 2,400 kJ/kg for optimal surface wettability (~10 min treatment), 4,800 kJ/kg for full oxygen saturation (~20 min treatment), reported for PE powder under pulsed magnetron microwave discharge.

Table 7. Plasma energy scenarios (basis: 0.701 kg/s PE feed)

Scenario	Specific energy (kJ/kg)	Power required (kW)
Optimal wettability	2,400	2400 × 0.701 = **1,682.4 ≈ 1,680**
Full O-saturation	4,800	4800 × 0.701 = **3,364.8 ≈ 3,360**

4.9 Calculated Stage Energy-Duty Balance

Table 8. Energy balance summary

Stage	Heat duty (kW)
I — Plasma (optimal wettability scenario)	+1,680.00
I — Plasma (full saturation scenario)	+3,360.00
II — Gasification (E4)	−9,805.03
III — HT-WGS (E1)	+378.15
III — LT-WGS (E2)	+261.81
IV — PSA (E3)	+0.26

Summed stage duty

For the optimal plasma treatment condition:

$E_{net,optimal}$ = 1680.00 − 9805.03 + 378.15 + 261.81 + 0.26 = −7,484.81 kW

For the full-saturation plasma treatment condition:

$E_{net,full\ sat}$ = 3360.00 − 9805.03 + 378.15 + 261.81 + 0.26 = −5,804.81 kW

By sign convention (positive = energy consumed, negative = energy released), the summed stage duty is negative under both plasma-energy scenarios, indicating that the modeled exothermic thermal duties exceed the explicitly included energy inputs under the adopted sign convention.

5. Results

5.1 Stage II — Gasification Product Distribution

Stage II represents the principal conversion step of the proposed process, in which the PE-equivalent feed is subjected to oxygen-limited oxidative gasification at 773.15 K and 101,325 Pa. The RGIBBS equilibrium calculation predicts conversion of the ethylene surrogate into a product gas dominated by CH_4, CO_2, and CO, with H_2 and H_2O as additional products. The resulting Stream 17 composition is summarized in Table 9 and presented graphically in Figure 3.

Table 9. RGIBBS-1 output composition (Stream 17), mole fraction basis

Species	Mole fraction	mol %

CH_4	0.4055	40.55
CO_2	0.2943	29.43
CO	0.2057	20.57
H_2	0.0738	7.38
H_2O	0.0207	2.07
C_2H_4 (unreacted)	~0	—
O_2 (unreacted)	~0	—

Heat duty (E4): **−9,805.03 kW** (exothermic).

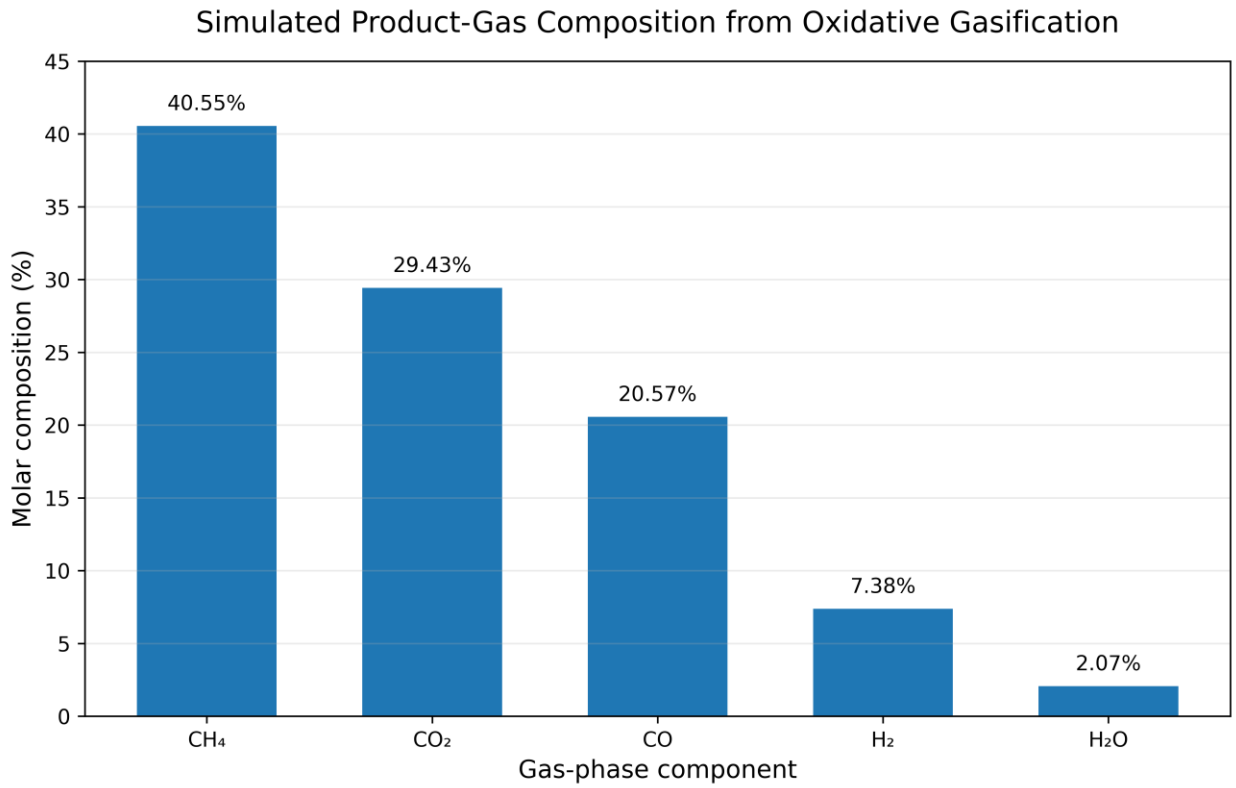


Figure 3. Simulated product-gas composition from the Stage II oxidative gasification reactor (Stream 17), expressed on a molar basis.

The simulated product gas was dominated by CH_4 (40.55 mol%), followed by CO_2 (29.43 mol%) and CO (20.57 mol%), while H_2 accounted for 7.38 mol% and H_2O for 2.07 mol%. The relatively high CH_4 fraction indicates that the selected equilibrium conditions favor

substantial formation of reduced carbon products, while the presence of CO and H_2 provides the reactive syngas components subsequently processed by the WGS stage. Accordingly, the Stage II outlet provides the feed basis for the downstream hydrogen-enrichment and CO_2-recovery steps.

5.2 Stage III — Water-Gas Shift Performance

Table 10. CO reduction across WGS stages

Point	CO content	Basis
Stage II outlet (pre-WGS)	20.57 mol%	Stream 17
After RCONV-1 (HT-WGS, 90% conv.)	1.369mol%	Stream 6, recorded HT-WGS outlet composition
After RCONV-2 (LT-WGS, 90% conv.)	0.114 mol% (Stream 14)	Stream 10, recorded LT-WGS outlet composition

*The intermediate HT-WGS outlet CO concentration is calculated from the specified 90% single-pass conversion and was not independently confirmed against the live DWSIM intermediate stream. The LT-WGS outlet CO concentration is taken from the recorded Stream 10 composition.

Heat loads reported by DWSIM for the baseline case: RCONV-1 (E1) = −378.15 kW; RCONV-2 (E2) = −261.813 kW.

5.3 Stage IV — PSA- Equivalent Product Streams

Table 11. Final separated stream compositions, mole fraction basis

Species	Stream 14 (H_2-rich)	Stream 15 (CO_2-rich)
H_2	0.5036	0.0108
CH_4	0.3875	0.1583
H_2O	0.0594	0.4608
CO_2	0.0476	0.3693
CO	0.00197	0.0008

Heat duty (E3, CS-1): **+0.26 kW**.

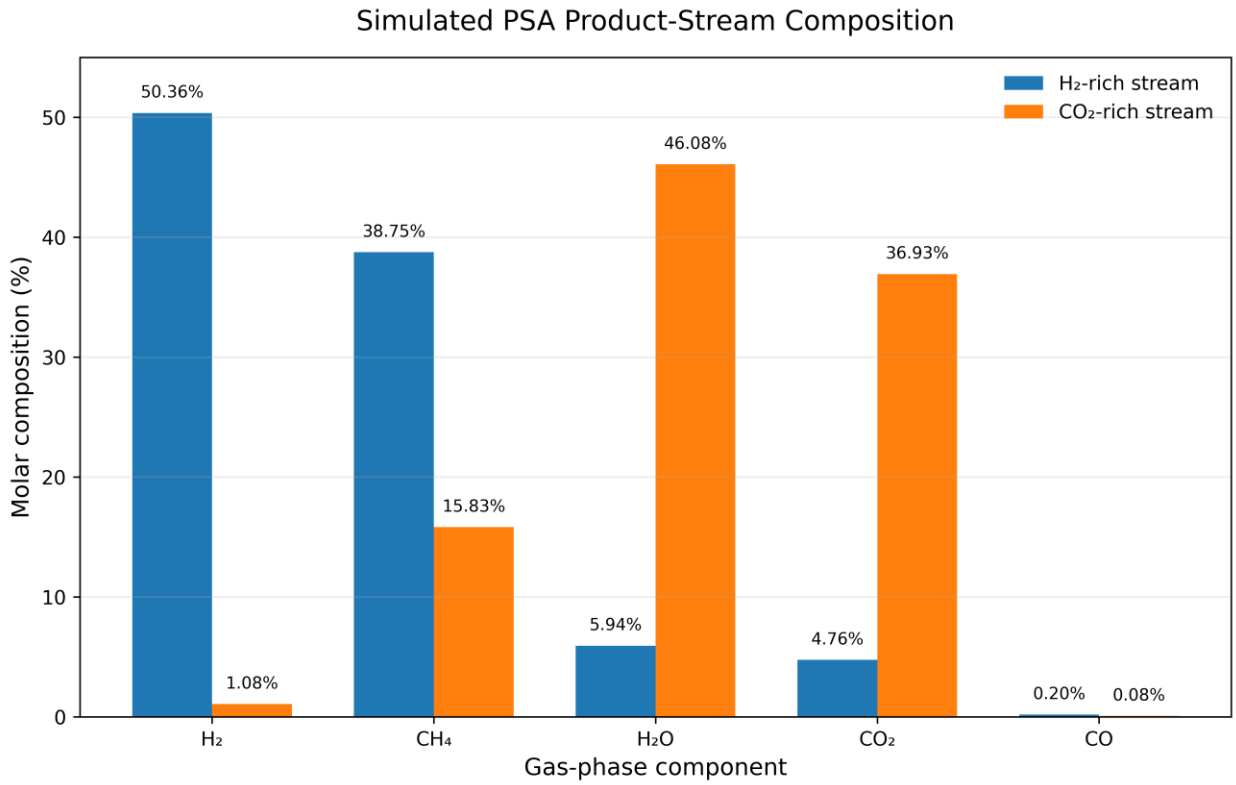


Figure 4. Simulated composition of the two PSA product streams on a molar basis. Stream 14 represents the H2-rich separator stream, while Stream 15 is the CO2-rich stream routed to downstream CO2 capture.

Stream 15 had a total flow of 70.7307 mol/s (1.91942 kg/s), confirmed directly from the live DWSIM file. Stream 14 had a total flow of 28.89 mol/s (0.302 kg/s), also confirmed directly from the live DWSIM file. The elemental carbon and hydrogen balances across Stages II–IV were independently checked and agreed to within 0.01%, providing an additional consistency check on the reported stream flows.

5.4 Stage V — CO_2 Capture

Table 12. $Ca(OH)_2$ slurry mass balance

Stream	Flow(kg/s)
CO_2 (in)	1.150
$Ca(OH)_2$ (in)	1.932

$CaCO_3$ (out)	2.611
H_2O (out)	0.471

Balance closure: 3.082 kg/s in = 3.082 kg/s out.

5.5 Stage VI — Heavy Metal Precipitation

Table 13. Contaminant removal and dosing (basis: 0.701 kg/s PE feed)

Metal	Feed flow (g/s)	Precipitate	Precipitate flow (g/s)
Zn	0.2561	$Zn(OH)_2$	0.3895
Cu	0.1289	$Cu(OH)_2$	0.1980
Pb	0.0070	$Pb(OH)_2$	0.0082
Total	**0.3920**		**0.5957**

Reagent required: NaOH = 0.4785 g/s (or $Ca(OH)_2$ = 0.4432 g/s as alternative).

Cd and Cr are not included in the selected quantitative contamination basis.

5.6 Calculated Stage Energy –Duty Balance

Table 14. Stage-wise heat duties and net balance

Stage	Heat duty (kW)	Sign convention
I — Plasma (optimal wettability)	+1,680.00	consumed
I — Plasma (full O-saturation, alt.)	+3,360.00	consumed
II — Gasification	−9,805.03	released
III — HT-WGS	+378.15	consumed
III — LT-WGS	+261.81	consumed
IV — PSA	+0.26	consumed
Net (optimal wettability scenario)	**−7,484.81**	**net thermal release**
Net (full saturation scenario)	**−5,804.81**	**net thermal release**

The summed stage duty is negative under both plasma-energy scenarios considered because the modeled exothermic duty of Stage II exceeds the explicitly included energy inputs and other stage duties. This result represents a negative summed thermal-duty estimate under the adopted sign convention; it does not demonstrate net electrical power export because thermal recovery and electrical conversion were not modeled.

5.7 Selected Process Stream and Material Accounting

Table 15. Selected feed, process, and product streams (basis: 0.701 kg/s PE-equivalent feed)

Input	Flow (kg/s)	Output	Flow (kg/s)
PE-equivalent (C_2H_4)	0.701	H_2-rich product (Stream 14)	0.302
O_2 (Stage II)	0.720	$CaCO_3$ (solid, recovered; Stage V)	2.614271428
Steam (Stage III, both additions)	0.800	H_2O (Stage V byproduct)	0.470668110
$Ca(OH)_2$ (Stage V)	1.935172047	Metal hydroxide precipitate (Stage VI)	0.0006
NaOH (Stage VI)	0.0005		

Note: Stream 15 (CO_2-rich stream) is an intermediate process stream entering Stage V and is not listed as a final output. The $Ca(OH)_2$ requirement, $CaCO_3$ production, and reaction-generated H_2O flow were calculated stoichiometrically from the DWSIM-reported CO_2 mass flow in Stream 15 (1.1495063 kg/s), using the molar masses listed in Table 4. This table presents selected feed and product streams and does not represent a complete overall process mass balance.

5.8 HT-WGS Temperature Sensitivity Results

An additional sensitivity case was simulated by reducing the high-temperature water-gas shift (HT-WGS) reactor outlet temperature from 773.15 K to 700 K (426.85 °C), while maintaining the specified HT-WGS conversion at 90%. The low-temperature water-gas shift (LT-WGS) reactor outlet temperature and specified conversion were retained at 473.15 K and 90%, respectively. The remaining model configuration and operating specifications were kept unchanged.

The HT-WGS reactor heat load reported by DWSIM was −378.15 kW for the baseline case at 773.15 K and −659.334 kW for the 700 K sensitivity case. The corresponding reactor

temperature differences were 0.0517439 K and −73.0983 K, respectively. The total molar flow of Stream 6 was 82.9707 mol s^{-1} in both recorded cases. The downstream stream-flow records were also comparable between the baseline and sensitivity cases. The principal simulation settings and recorded HT-WGS results are summarized in Table X.

Table 16. Baseline and reduced-temperature HT-WGS simulation results.

Parameter	Baseline case	Sensitivity case
HT-WGS outlet temperature (K)	773.15	700.00
Specified HT-WGS conversion (%)	90	90
HT-WGS temperature difference (K)	0.0517439	−73.0983
HT-WGS heat load (kW)	−378.15	−659.334
Stream 6 total molar flow (mol s^{-1})	82.9707	82.9707
LT-WGS outlet temperature (K)	473.15	473.15
Specified LT-WGS conversion (%)	90	90

Note: Conversion values are specified model inputs. Heat-load signs are reported as displayed by DWSIM. Table 16 compares the baseline and sensitivity-case records; it does not represent experimental validation.

6. Discussion

6.1 Revision of the Plasma Pretreatment's Mechanistic Role

An earlier iteration of this design attributed Stage II's CO content to oxygen introduced during Stage I plasma treatment, on the basis that plasma-induced surface oxidation (–OH, C=O, –COOH groups) could supply the oxygen subsequently incorporated into CO during thermal decomposition. This was tested against the process's own elemental mass balance and found untenable: accounting for the full CO output of Stage II would require approximately 228.6 g/s of oxygen, whereas plasma surface functionalization is a monolayer-scale phenomenon capable of supplying oxygen several orders of magnitude below this quantity. The process formulation was accordingly revised: Stage I is treated as a surface-activation step that may influence subsequent thermal reactivity, while all oxygen required for Stage II is supplied explicitly as a metered gasification input. This revision is presented here deliberately, rather than omitted, since the same mass-balance check is one a reviewer would be expected to perform.

6.2 Stage II Product Distribution Relative to Literature Benchmarks

The equivalence ratio selected for this work (ER = 0.30, Section 4.2) represents a deliberate process-design choice within the range investigated in plastic gasification studies. Because reported favorable ER values depend on feedstock, oxidant, temperature, reactor configuration, and the performance metric considered, ER = 0.30 is treated here as the operating basis for the integrated process rather than as a universal optimum. The simulated product's high CH_4 content (40.55 mol%, Table 9) is consistent with literature describing oxygen-gasified PE specifically as CH_4-enriched relative to other feedstocks, consistent with the methane formation observed under some oxygen-gasification conditions for polyethylene-containing feeds [16-20].

However, direct comparison against reported PE syngas compositions shows this work's CO (20.57 mol%) and H_2 (7.38 mol%) yields running lower, and CH_4 correspondingly higher, than several literature benchmarks — for example, reported PE gasification compositions of 76.2% H_2/8.53% CO/10.9% CH_4 under one set of conditions, and 49.21% H_2/21.7% CO/12.78% CH_4 under a plasma-assisted co-gasification study. This work's Stage II is modeled as a Gibbs free-energy equilibrium calculation under a Vapor Only phase constraint (Section 4.3); it therefore represents a thermodynamic idealization of complete gas-phase conversion at the specified temperature and ER, rather than a kinetically-limited real reactor outcome. Real gasifiers are constrained by residence time, mixing, and heat transfer in ways an equilibrium model does not capture, and the specific benchmarks cited operate at different oxidant compositions, feedstock forms, and possibly different ER than modeled here [16-20]. The differences between the present prediction and published gas compositions cannot be attributed to a single factor because the reported studies employ different temperatures, oxidants, reactor configurations, feedstock forms, and operating conditions. These differences illustrate the importance of treating the present Stage II result as the equilibrium prediction for the selected process conditions rather than as a direct reproduction of any individual experimental gasifier.

6.3 Water-Gas Shift Operating Conditions

The two-stage WGS configuration adopted in this work (Section 3.3, Section 4.4) matches standard industrial practice in architecture. Two specific parameters diverge from typical literature values. First, the high-temperature stage operates at 773.15 K (500°C), above the commonly cited industrial range of 310-450°C for iron-oxide/chromium-oxide catalysts. Second, the 90% single-pass conversion assumed for each stage is higher than the conversion reported for at least one high-temperature WGS catalyst. Lee et al. reported a

CO conversion of 64% at 400°C for a Cr-free Fe/Ni catalyst, approaching the corresponding equilibrium conversion of 65% [23].

Despite these deviations, the resulting outlet CO concentrations are numerically comparable with commonly reported target ranges for two-stage WGS operation [21-23]. The elevated HT-WGS temperature's effect on catalyst longevity and side-reaction selectivity was not modeled in this work and is noted as an area for future refinement. To further examine the effect of the selected HT-WGS operating temperature within the configured process model, an additional sensitivity case at 700 K was evaluated. The results and limitations of this comparison are discussed in the following subsection.

6.4 Interpretation and Limitations of the HT-WGS Temperature Sensitivity Analysis

Reducing the specified HT-WGS outlet temperature from 773.15 K to 700 K changed the calculated reactor heat load from −378.15 kW to −659.334 kW under the sign convention reported by DWSIM. This difference represents a change in the simulated reactor duty; it should not, by itself, be interpreted as an improvement in energy efficiency, a reduction in overall process energy demand, or an increase in recoverable energy. The individual reactor duty is also distinct from the summed stage duty used in the overall process energy assessment.

The specified HT-WGS and LT-WGS conversions were both retained at 90%. Consequently, the sensitivity case evaluates the response of the configured process model to a change in the HT-WGS temperature specification, rather than predicting conversion from independently modelled catalyst kinetics. It therefore does not establish that the specified conversion would be experimentally achievable at 700 K.

The recorded outlet-stream compositions for the sensitivity case were similar to the previously recorded baseline values. Accordingly, the present comparison does not establish a measurable improvement in carbon monoxide removal, hydrogen recovery, or product-stream purity. The analysis is limited to a single alternative HT-WGS temperature and does not constitute a comprehensive operating-temperature optimization or experimental validation. These limitations should be considered when interpreting the sensitivity results alongside the broader process simulation and energy assessment.

6.5 Applicability of Stage V Benchmarks to This Work's CO_2 Concentration

The lime-slurry CO_2 capture literature cited in support of Stage V (Section 2.5) was obtained under CO_2 concentrations of 8.5% or lower, substantially below this work's Stream 15 CO_2 content of 36.93% (Table 11) [24-25]. Carbonation reactions of this type are generally expected to proceed more readily at higher CO_2 partial pressure, the higher CO_2 concentration in the present Stream 15 provides a different operating basis from the cited studies. The literature therefore supports the feasibility of $Ca(OH)_2$-based carbonation as a process option, but the cited capture performance should not be directly transferred to the present stream without experimental or detailed reactor-level evaluation. This expectation is not independently confirmed by literature specific to this concentration range and is presented as a reasoned inference rather than a validated result.

6.6 Vapor-Phase-Only Assumption in Stage II

The Gibbs reactor used to model Stage II was configured under a 'Vapor Only' reactive phase constraint. This configuration was adopted because the inclusion of solid carbon in the available equilibrium formulation produced a solver-dependent result in which the solid phase remained effectively unreacted. The present model therefore uses a vapor-phase representation and does not explicitly resolve char or soot formation. Consequently, the reported Stage II composition should be interpreted as the equilibrium gas-phase prediction under the selected model constraints rather than as a complete prediction of all carbon-containing products.

6.7 Modeling and Data Verification Limitations

The Stream 14 total molar flow rate (28.8925 mol/s; 0.30193 kg/s) was confirmed directly from the DWSIM stream export. The combined WGS steam addition was 0.80 kg/s, comprising 0.50 kg/s in Stream 2 and 0.30 kg/s in Stream 8. Carbon and hydrogen balance checks were reconstructed from the exported stream flow rates and compositions; however, the original independent calculations underlying the previously reported agreement of 0.01% were not available for direct verification. Accordingly, the 0.01% agreement is not claimed as an independently verified result. The plasma energy requirements presented in Section 4.8 were calculated by scaling the reported batch-process specific energy requirement (0.25 kg/batch) to the continuous feed basis used in this study. This scaling assumes that the specific energy requirement is transferable from the reported batch treatment to the continuous process basis. The two plasma-energy scenarios considered both result in a negative summed stage duty (Table 14). This

indicates that the modeled exothermic thermal duty exceeds the explicitly included energy inputs under the adopted sign convention; it should not be interpreted as direct net electrical power export because thermal recovery and electrical conversion were not modeled. Accordingly, the calculated energy values should be interpreted as process-model estimates based on the adopted specific-energy scaling basis.

6.8 Heavy Metal Contamination Coverage

The heavy-metal dosing calculation in Stage VI (Section 4.7) accounts for zinc, copper, and lead, for which PE-specific contamination data were identified (Section 2.6). Cadmium and chromium are not included in the quantitative dosing calculation, although their occurrence in plastic materials has been reported [5-6]. The present calculation is therefore restricted to the selected Zn, Cu, and Pb contamination basis.

7. Conclusion

This work presents a closed-loop, six-stage process design (plus one optional stage) for the destruction and resource recovery of polyethylene microplastics, integrating cold plasma pretreatment, oxidative gasification, two-stage water-gas shift, pressure-swing adsorption, lime-based CO_2 capture, and heavy-metal precipitation. Each individual unit operation draws on established literature precedent (Section 2) [12-13 , 16-26]; the contribution of this work lies in their specific end-to-end integration for PE microplastics as feedstock, evaluated through process simulation with stage-wise material and energy-duty accounting. This specific assembly was not identified in the literature surveyed for this study.

The simulated process converts a 0.701 kg/s PE-equivalent feed into a hydrogen-containing product stream (50.36 mol% H_2), 2.611 kg/s of recoverable solid $CaCO_3$, and 0.596 g/s of precipitated heavy-metal hydroxides, while producing a negative summed stage duty under both plasma-energy scenarios considered (−7,484.81 kW and −5,804.81 kW). These results follow the correction of a mechanistically unsound assumption identified during development of the process model, in which plasma pretreatment had initially been treated as the source of oxygen responsible for CO formation in Stage II. Elemental mass-balance analysis demonstrated that this assumption was inconsistent with the modeled process, and the formulation was subsequently corrected by introducing a metered oxidative-gasification oxygen input, consistent with the equivalence-ratio basis discussed in Sections 2.3 and 6.1. This correction forms part of the documented model-development process and illustrates the importance of explicitly testing process assumptions against elemental balances.

The results represent a process-simulation study based on an equilibrium gasification model, specified WGS conversions, an idealized gas-separation representation, stoichiometric precipitation calculations, and a scaled plasma-energy basis. The principal remaining development requirements are experimental confirmation of the precipitation stages, detailed PSA and reactor modeling, direct verification of the selected process streams, and evaluation of plasma-energy scale-up and membrane performance.

Future work includes bench-scale confirmation of the $CaCO_3$ and metal-hydroxide precipitation chemistry proposed here; extension of the heavy-metal contamination basis to include cadmium and chromium; and evaluation of H_2/CH_4 carryover from the PSA stage (Section 5.3) in conjunction with a downstream reforming step, which could potentially increase hydrogen recovery beyond that obtained from the water-gas shift stages alone. Further development should also evaluate heat recovery between exothermic and energy-demanding process stages to determine the practical energy efficiency of the integrated system.

References

[1] Lambert, S.; Sinclair, C.; Boxall, A. Occurrence, Degradation, and Effect of Polymer-Based Materials in the Environment. Reviews of Environmental Contamination and Toxicology 2014, 227, 1–53. DOI: 10.1007/978-3-319-01327-5_1.

[2] Al Harraq, A.; Brahana, P. J.; Arcemont, O.; Zhang, D.; Valsaraj, K. T.; Bharti, B. Effects of Weathering on Microplastic Dispersibility and Pollutant Uptake Capacity. ACS Environmental Au 2022, 2(6), 549–555. https://doi.org/10.1021/acsenvironau.2c00036.

[3] Sołowski, G.; Shalaby, M.; Özdemir, F. A. Plastic and Waste Tire Pyrolysis Focused on Hydrogen Production—A Review. Hydrogen 2022, 3(4), 531–549. DOI: 10.3390/hydrogen3040034.

[4] Diaz-Silvarray, L. S.; Zhang, K.; Phan, A. N. Monomer Recovery through Advanced Pyrolysis of Waste High Density Polyethylene (HDPE). Green Chemistry 2018, 20(8), 1813–1823. https://doi.org/10.1039/C7GC03662K.

[5] Jiang, Y.; Song, G.; Zhang, H. Material Identification and Heavy Metal Characteristics of Plastic Packaging Bags Used in Chinese Express Delivery. Frontiers in Environmental Science 2023, 11, 1253108. DOI: 10.3389/fenvs.2023.1253108.

[6] Alam, O.; Yang, L.; Yanchun, X. Determination of the Selected Heavy Metal and Metalloid Contents in Various Types of Plastic Bags. Journal of Environmental Health Science and Engineering 2019, 17, 161–170. DOI: 10.1007/s40201-019-00337-2.

[7] Gao, X.; Hassan, I.; Peng, Y.; Huo, S.; Ling, L. Behaviors and Influencing Factors of the Heavy Metals Adsorption onto Microplastics: A Review. Journal of Cleaner Production 2021, 319, 128777. DOI: 10.1016/j.jclepro.2021.128777.

[8] Mehmood, T.; Mustafa, B.; Mackenzie, K.; Ali, W.; Sabir, R. I.; Anum, W.; Gaurav, G. K.; Riaz, U.; Liu, X.; Peng, L. Recent Developments in Microplastic Contaminated Water Treatment: Progress and Prospects of Carbon-Based Two-Dimensional Materials for Membranes Separation. Chemosphere 2023, 316, 137704. https://doi.org/10.1016/j.chemosphere.2022.137704.

[9] Sun, J.; Xiong, Y.; Jia, H.; Han, L.; Yin, K. Superb Microplastics Separation Performance of Graphene Oxide Tuned by Laser Bombardment. Journal of Hazardous Materials 2024, 461, 132599. https://doi.org/10.1016/j.jhazmat.2023.132599.

[10] Mi, K.; Chang, D.; Zhang, L.; Lv, J.; Liu, Y.; Cheng, M.; Hou, S. MXene and Silver Intercalated Graphene Oxide Membrane with Antibacterial Performance for High-Permeability Micro/Nanoplastics Removal. Journal of Environmental Chemical Engineering 2026, 14(5), 124015. https://doi.org/10.1016/j.jece.2026.124015.

[11] Arenas-Blanco, B. A.; López-Meza, A.; Vesga-Gamboa, L. C.; Beltrán-Larrotta, J.-I.; Cajicá-Trillos, C. A.; Mejía-Ospino, E. Mechanistic Study of Nanoplastic Capture Using Functionalized Graphene Oxide: A Molecular Dynamics Approach. *Computational Materials Science* 2026, *265*, 114530. https://doi.org/10.1016/j.commatsci.2026.114530.

[12] Šourková, H.; Primc, G.; Špatenka, P. Surface Functionalization of Polyethylene Granules by Treatment with Low-Pressure Air Plasma. Materials 2018, 11(6), 885. https://doi.org/10.3390/ma11060885.

[14] Li, W.; Wu, W.; Li, Z. Controlling Interlayer Spacing of Graphene Oxide Membranes by External Pressure Regulation. ACS Nano 2018, 12(9), 9309–9317. https://doi.org/10.1021/acsnano.8b04187.

[13] Šourková, H.; Špatenka, P. Plasma Activation of Polyethylene Powder. Polymers 2020, 12(9), 2099. https://doi.org/10.3390/polym12092099.

[15] Liu, T.; Tian, L.; Graham, N.; Yang, B.; Yu, W.; Sun, K. Regulating the Interlayer Spacing of Graphene Oxide Membranes and Enhancing Their Stability by Use of PACl. Environmental Science & Technology 2019, 53(20), 11949–11959. https://doi.org/10.1021/acs.est.9b04418.

[16] Du, Y.; Yang, Q.; Berrouk, A. S.; Yang, C.; Al Shoaibi, A. S. Equivalent Reactor Network Model for Simulating the Air Gasification of Polyethylene in a Conical Spouted Bed Gasifier. *Energy & Fuels* 2014, *28*(11), 6830–6840. https://doi.org/10.1021/ef501667n.

[17] Hasanzadeh, R.; Mojaver, M.; Azdast, T.; Park, C. B. Polyethylene Waste Gasification Syngas Analysis and Multi-Objective Optimization Using Central Composite Design for Simultaneous

Minimization of Required Heat and Maximization of Exergy Efficiency. Energy Conversion and Management 2021, 247, 114713. DOI 10.1016/j.enconman.2021.114713.

[18] Ghenai, C. Combustion and Emissions Performance of Syngas Fuels Derived from Palm Kernel Shell and Polyethylene (PE) Waste via Catalytic Steam Gasification. *Combustion* **2015**, *1*, 61291.

[19] Yousef, S.; Tamošiūnas, A.; Aikas, M.; Uscila, R.; Gimžauskaitė, D.; Zakarauskas, K.; et al. Plasma Steam Gasification of Surgical Mask Waste for Hydrogen-Rich Syngas Production. International Journal of Hydrogen Energy 2024. DOI: 10.1016/j.ijhydene.2023.09.288.

[20] Ciuffi, B.; Chiaramonti, D.; Rizzo, A. M.; Frediani, M.; Rosi, L. A Critical Review of SCWG in the Context of Available Gasification Technologies for Plastic Waste. Applied Sciences 2020, 10(18), 6307. DOI: 10.3390/app10186307.

[21] Patel, R.; Varatharajan, P.; Zhang, Q.; Li, Z.; Gu, S. Catalysts in the Water-Gas Shift Reaction: A Comparative Review of Industrial and Academic Contributions. *Carbon Capture Science & Technology* **2025**, *15*, 100388. https://doi.org/10.1016/j.ccst.2025.100388.

[22] Ladebeck, J. R.; Wagner, J. P. Catalyst Development for Water-Gas Shift. In *Handbook of Fuel Cells – Fundamentals, Technology and Applications*, Vol. 3, Part 2, pp. 190–201; Wiley, 2003. https://doi.org/10.1002/9780470974001.f302017.

[23] Lee, D.-W.; Lee, M.-S.; Lee, J.-Y.; Kim, S.; Eom, H.-J.; Moon, D.-J.; Lee, K.-Y. The Review of Cr-Free Fe-Based Catalysts for High-Temperature Water-Gas Shift Reactions. *Catalysis Today* **2013**, *210*, 2–9. https://doi.org/10.1016/j.cattod.2012.12.012.

[24] Criado, Y. A.; García, R.; Abanades, J. C. Demonstration of CO_2 Capture with CaO and $Ca(OH)_2$ in a Countercurrent Moving Bed Carbonator Pilot. Chemical Engineering Journal 2024, 494, 152945. https://doi.org/10.1016/j.cej.2024.152945.

[25] Nejad, P. M. G.; Hatamipour, M. S. Investigation on the Removal of Carbon Dioxide Exhausted from Industrial Units in a Lab-Scale Fluidized Bed Reactor. *Bulletin of Chemical Reaction Engineering & Catalysis* **2020**, *15*(2), 579–590. https://doi.org/10.9767/bcrec.15.2.7882.579-590.

[26] Chen, Q.; Yao, Y.; Li, X.; Lu, J.; Zhou, J.; Huang, Z. Comparison of Heavy Metal Removals from Aqueous Solutions by Chemical Precipitation and Characteristics of Precipitates. Journal of Water Process Engineering 2018, 26, 289–300. DOI: 10.1016/j.jwpe.2018.11.003.